

Gemini Frontier Fields: Wide-field Adaptive Optics K_s -band Imaging of the Galaxy Clusters MACS J0416.1-2403 and Abell 2744¹

M. Schirmer¹, E. R. Carrasco¹, P. Pessev¹, V. Garrel¹, C. Winge¹, B. Neichel^{2,1}, F. Vidal^{3,1}

¹*Gemini Observatory, Casilla 603, La Serena, Chile*

²*Aix Marseille Université, CNRS, Laboratoire d'Astrophysique de Marseille, UMR 7326, 13388, Marseille, France*

³*Observatoire De Paris, Place Jules Janssen, 92190 Meudon, France*

mschirme@gemini.edu

ABSTRACT

We have observed two of the six Frontier Fields galaxy clusters, MACS J0416.1-2403 and Abell 2744, using the Gemini Multi-Conjugate Adaptive Optics System (GeMS) and the Gemini South Adaptive Optics Imager (GSAOI). With $0''.08$ – $0''.10$ FWHM our data are nearly diffraction-limited over a $100'' \times 100''$ wide area. GeMS/GSAOI complements the *Hubble Space Telescope* (*HST*) redwards of $1.6\mu\text{m}$ with twice the angular resolution. We reach a 5σ depth of $K_s \sim 25.6$ mag (AB) for compact sources. In this paper we describe the observations, the data processing and the initial public data release. We provide fully calibrated, co-added images matching the native GSAOI pixel scale as well as the larger plate scales of the *HST* release, adding to the legacy value of the Frontier Fields. Our work demonstrates that even for fields at high galactic latitude, where natural guide stars are rare, current multi-conjugated adaptive optics technology at 8m-telescopes has opened a new window on the distant Universe. Observations of a third Frontier Field, Abell 370, are planned.

Subject headings: Techniques: image processing, Instrumentation: adaptive optics, Galaxies: Clusters: individual (MACS J0146.1-2403, Abell 2744)

1. Introduction

Strong gravitational lensing by massive clusters of galaxies provides us with magnified views of high redshift galaxies in the young Universe. The *HST* Frontier Fields campaign observes six strong lensing clusters in the $0.43 - 1.6 \mu\text{m}$ wavelength range, using the Advanced Camera for Surveys (*ACS*) and the Wide Field Camera 3 (*WFC3*). Complementary observations have been obtained with Chandra (PI:

Murray, S.), Spitzer (PIs: Soifer, T., Capak, P.), Subaru (Postman et al. 2011), the VLT (Owers et al. 2011) and the AAT (Ebeling et al. 2014).

HST/WFC3 is sensitive to near-infrared radiation shorter than $1.7\mu\text{m}^2$. This design was chosen (1) to allow for simpler thermo-electric cooling of the detector, and (2) because *HST* itself contributes significantly to the thermal background and thus would offer only a small gain with respect to ground-based observatories at $\gtrsim 2\mu\text{m}$. While the Earth's atmosphere has a suitable observing window between $2.0\mu\text{m}$ and $2.3\mu\text{m}$ (K_s -band), its turbulence limits the resolution and the depth with classical imaging. Using multi-conjugated adaptive optics (MCAO) (Ragazzoni et al. 2000; Ellerbroek & Rigaut 2000), these adverse effects can be overcome for fields as large as one arcminute or more. In theory, diffraction limited observations are possi-

¹**Based on observations** obtained at the Gemini Observatory, which is operated by the Association of Universities for Research in Astronomy, Inc., under a cooperative agreement with the NSF on behalf of the Gemini partnership: the National Science Foundation (United States), the Science and Technology Facilities Council (United Kingdom), the National Research Council (Canada), CONICYT (Chile), the Australian Research Council (Australia), Ministério da Ciência, Tecnologia e Inovação (Brazil) and Ministerio de Ciencia, Tecnología e Innovación Productiva (Argentina). **Based on observations** made with ESO Telescopes at the La Silla and Paranal Observatories, Chile.

²http://www.stsci.edu/hst/nicmos/documents/handbooks/current_NEW/c04_imaging.6.8.html

Table 1: Summary of the observing nights as of February 2015

Target	Night (UT)	Exposures	\langle AO seeing \rangle	Nat. seeing
MACS J0416.1-2403	2014-01-13	40×120 s	0".076	0".4–0".7
MACS J0416.1-2403	2014-01-14	37×120 s	0".077	0".6–0".9
MACS J0416.1-2403	2014-01-19	34×120 s	0".175	0".9–1".1
MACS J0416.1-2403	2014-01-20	47×120 s	0".103	0".5–0".9
MACS J0416.1-2403	2014-01-22	16×120 s	0".105	0".5–0".7
Abell 2744	2014-09-07	40×120 s	0".110	0".7–1".2

ble, given a sufficient number of bright natural guide stars (NGS) and a good laser return for the artificial laser guide stars (LGS). Nowadays, such wide-field diffraction limited observations can be obtained in the near-infrared at Gemini South with GeMS³ (Rigaut et al. 2014; Neichel et al. 2014b) and the GSAOI⁴ (McGregor et al. 2004; Carrasco et al. 2012) camera.

GeMS is the first MCAO system in use at an 8m telescope. It delivers uniform and nearly diffraction-limited images over a 2' field at near-infrared wavelengths. GeMS uses five sodium LGS and needs three NGS to compensate for tip-tilt and focus, reducing plate-dynamical errors (plate scale variations). To achieve optimum performance, the NGS should be positioned as close as possible to an equilateral triangle around the science target. Best constellations (*asterisms*) are the ones that cover most of the field. The larger the angular separations between the stars, then the lower the plate scale error will be over the imaged field. Unfortunately, this condition is usually not met at high galactic latitude where the stellar density is low. With sub-optimal asterisms the PSF will become larger and non-uniform. Only one sufficiently bright NGS is available for each of our targets, yet we still achieve an image seeing of 100 milli-arcseconds or better.

The focus in the remainder of this paper is on the observations (Section 2), and on various data reduction aspects such as background modeling and astrometry (Section 3). In Section 4 we summarize the properties of the coadded images and describe the data release.

2. Observations

GSAOI is a near-infrared adaptive optics (AO) camera designed to work with GeMS. Its focal plane is formed by a 2×2 mosaic of Hawaii-2RG 2048×2048

pixel arrays with $2''.8$ – $3''.0$ wide gaps. Images are recorded in a $85'' \times 85''$ field of view with a plate scale of $0''.0197 \text{ pixel}^{-1}$. The K_s -band filter in GSAOI has 50% cut-on and cut-off wavelengths of $1.99\mu\text{m}$ and $2.31\mu\text{m}$, respectively. More details about GSAOI can be found on the instrument web page.

The GSAOI pointings for MACS J0416.1-2403, Abell 2744 and Abell 370 are shown in the Appendix (Figs. 10, 11 and 12, respectively). We have overlaid the currently available *HST* data, as well as the areas of highest strong lensing magnification for $z = 9$ sources as calculated by Richard et al. (2014). In case of Abell 2744 we cannot cover the area of highest magnification due to the large angular separation of the NGS from the cluster center.

MACS J0416.1-2403 was observed to the planned depth with GSAOI using director's discretionary time (Program ID: GS-2013B-DD-1). To optimize the observations, the NGS was located outside the GSAOI field of view, but within the patrol field area of GeMS. Due to a setup error (the NGS is a high proper motion star), the images observed during the first two nights were recorded with a South-Eastern offset of $24''$. As a result, the NGS appears in one of the four arrays. The images recorded during the other three nights have the correct base position.

Regular 3×3 dither patterns (repeated several times) with a step size of $7''$ were used to cover the gaps between the arrays. Processing of the data has revealed that this strategy does not allow to fully suppress background residuals and cross-talk (Sect. 3). Hence we switched to random dithers within a $14''$ wide box for Abell 2744 (and Abell 370), resulting in significantly improved background characteristics.

The observing log is presented in Table 1. The targets, dates, number of images and exposure times are listed in columns 1, 2 and 3, respectively. For the remainder of the Abell 2477 and Abell 370 data

³<http://www.gemini.edu/sciops/instruments/gems/>

⁴<http://www.gemini.edu/sciops/instruments/gsaoi/>

we will use 180s instead of 120s to reduce the overhead. Columns 4 and 5 show the average corrected AO FWHM within $1'$ of the NGS, and the natural seeing recorded by the DIMM, respectively. 2014-01-19 was significantly worse with an average AO-corrected seeing of $0''.17$. Data from that night was included in the low resolution stack, only (see Sect. 4). Observations for Abell 2744 have been started in September 2014 (Program ID: GS-2014B-DD-1, 25% complete by the time of writing). Abell 370 will follow in 2015.

3. Data reduction

Data processing was done with THELI (Schirmer 2013; Erben et al. 2005), following the example in Appendix B of Schirmer (2013). Specific treatments for the GSAOI data are motivated below.

3.1. Two-pass background modeling

To summarize, we have subtracted the median of 8 consecutive exposures to remove the background from the image sequences. This corresponds to a floating time window of 22 minutes duration. Windows of 15 – 30 minutes length yield good background correction as well. Shorter windows (5 or less images) cause artifacts near extended objects (insufficient statistics due to masking) and increased noise. Longer windows (e.g. 35 – 45 minutes) may undersample temporal variations in atmospheric emissivity, increasing the background residuals (see Sect. 3.3). Owing to its comparably small field of view, GSAOI is less sensitive to the latter effect than other near-infrared imagers.

The average background signal is 7490 ± 440 ADU or $12.58 \text{ mag arcsec}^{-2}$ (VEGA) in K_s -band. This is close to the long-term average of $12.62 \text{ mag arcsec}^{-2}$, including a thermal contribution of $\sim 0.7 \text{ mag arcsec}^{-2}$ from the warm MCAO enclosure (see also Sect. 3.3).

In the first step of the two-pass background subtraction, the exposures were median combined without masking to get rid of the bulk of the sky signal. During the second step, THELI applies *SExtractor* (Bertin & Arnouts 1996) to the corrected images from the first pass, computing mask images. Without these masks the fainter halos of the cluster galaxies bias the background model toward higher values, causing dark halos in the coadded image.

We have found that the *SExtractor* masks are too small. A module was added to THELI that optionally enlarges the masks. It uses an alternative parametrization of the best-fit ellipse to an object's isophotes. A

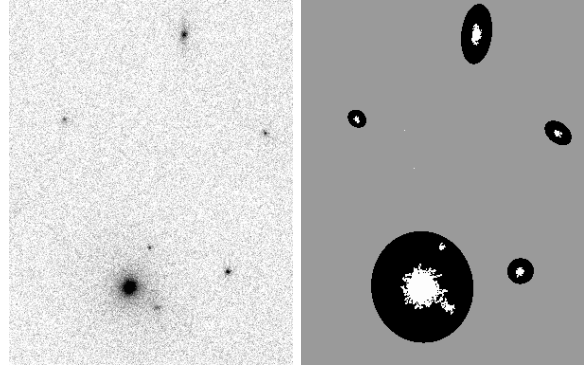


Fig. 1.— Expansion of object masks to avoid biasing of the background models by faint galaxy halos. Left: Part of a GSAOI image after first pass background modeling. Right: *SExtractor* mask before (white) and after (black) expansion with $R = 8$, using `DETECT.THRESH = 1.2` and `DETECT.MINAREA = 20`.

pixel with image coordinates x and y is located inside the ellipse if

$$C_{XX}(x - \bar{x})^2 + C_{YY}(y - \bar{y})^2 + C_{XY}(x - \bar{x})(y - \bar{y}) \leq R^2, \quad (1)$$

where \bar{x} and \bar{y} represent the object's centroid (first moment), and C_{XX} , C_{YY} and C_{XY} are *SExtractor* parameters calculated from the second brightness moments. A choice of $R \sim 3$ reproduces the outer isophote of a detection⁵. Only for $R = 8$ or higher the over-correction of the sky disappeared in the co-added images. This *mask expansion* is available in THELI as of v2.9.0, with R being referred to as the *mask expansion factor*. It can be selected during background modeling, collapse correction (see below), and individual sky subtraction. Figure 1 illustrates the effect.

Note that low surface brightness features larger than the dither box (such as intra-cluster light) escape this masking process and are suppressed in the co-added images. This can be avoided by interspersing blank sky fields into the observing sequence.

3.2. Reset anomaly and background gradients

GSAOI shows an unstable reset anomaly in array #2 for its medium and faint readout modes, probably due to a bias/dark problem in the detector controller. Every first image in an exposure series is affected by it, as well as the image taken immediately after an interruption (e.g. because of the laser being shuttered

⁵For details see the *SExtractor* user manual v2.13, Sect. 10.1.6)

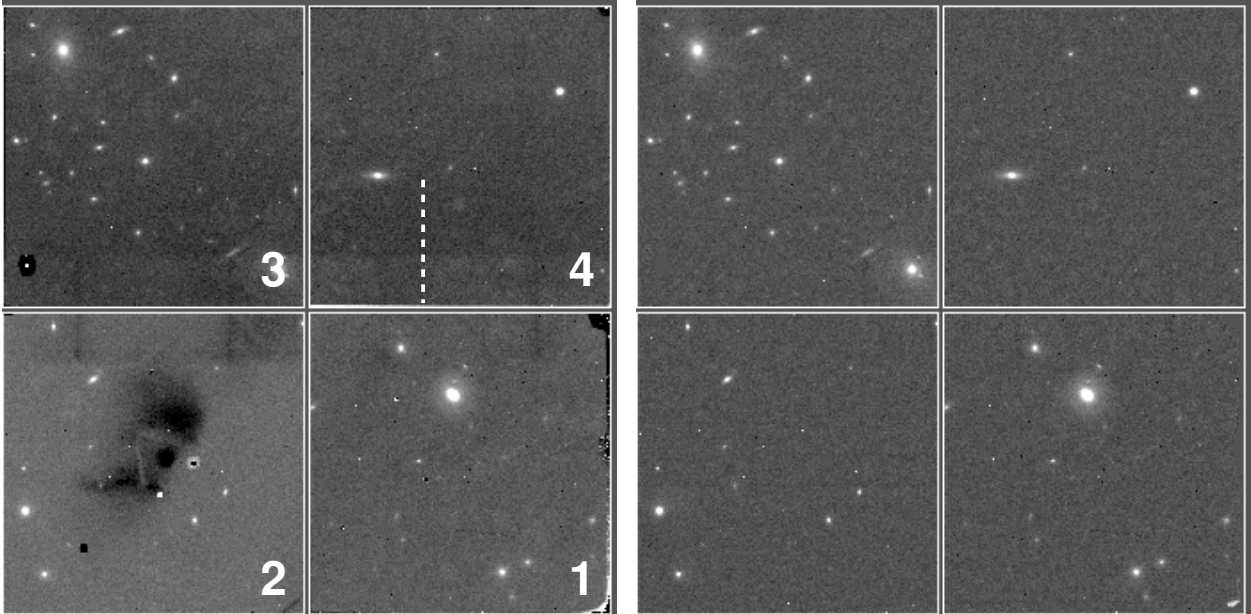


Fig. 2.— Left: The four GSAOI detector arrays (labeled). A reset anomaly (dark extended spot) appears in array #2 at the beginning of each observing sequence. Independently, horizontal striping with a low amplitude occurs in $\geq 80\%$ of exposures, affecting all four detectors. We illustrate the latter by plotting the mean row values along the dashed white line in array #4 both before and after correction (see Fig. 3). Right: Same exposure after correction for reset anomaly and striping. Note that this is a high contrast display of 12×12 binned data, exaggerating the effects.

for air planes or satellites). The anomaly is evident in the data after background subtraction. Figure 2 shows that we can correct it by subtracting a rescaled median model of the affected images. The rescaling factors (between 0.2 and 1.2) were determined manually.

In addition to the reset anomaly, and independent of it, horizontal stripes are found in 84% of the MACS J0416.1-2403 data (and to a lesser degree for Abell 2744). They run parallel to the interface between arrays #2/3 and #1/4 (see Figs. 2 and 3). Both the amplitude and the angular extent of the stripes vary between exposures. They affect an identical number of rows in all four arrays. The amplitude is much lower than the reset anomaly, in the worst case reaching 0.2% of the background level (3 – 4 times smaller than the sky noise). For deep coadded images this effect must be corrected for by subtracting an average column profile (*collapse correction* in THELI). The calculation of the profile includes object masking (see Sect. 3.1).

3.3. Sky subtraction

Background modeling with a floating median (Sect. 3.1) may leave residuals in the data due to undersam-

pled temporal variations of the sky. We correct individual exposures by masking all objects (Sect. 3.1), using a conservative mask expansion factor of $R = 20$. The masked images are convolved with a Gaussian and subtracted from their originals. For MACS J0416.1-2403, best results in terms of preserving faint extended galaxy halos while minimizing background inhomogeneities were obtained with a $3''$ wide kernel. Abell 2744 required a $6''$ kernel due to a few low surface brightness galaxies which were undetected (and thus unmasked) in individual exposures.

The coadded images (normalized to 1s exposure time) have a mean background level of zero. Without sky subtraction the normalized background value would be 62 ± 4 ADU. Effective gains are listed in the FITS headers. Note that due to the dithering of mosaiced data the total exposure time varies across the image. Local noise levels must be estimated using the coadded weight maps.

3.4. Image persistence and crosstalk

Saturated objects leave a weak imprint in subsequent GSAOI exposures (image persistence). In

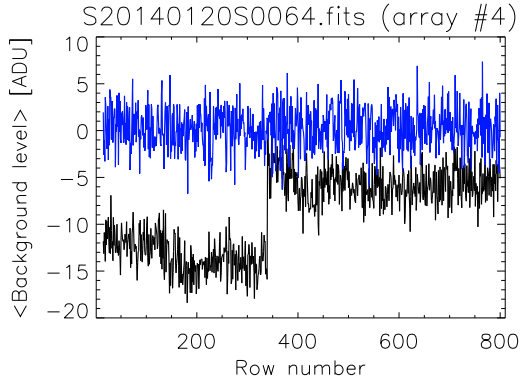


Fig. 3.— Mean row values before (black line) and after (blue line) correction for striping. The data was extracted along the dashed line shown in Fig. 2.

the case of MACS J0416.1-2403, the only saturating source is a bright field star (Fig. 10), leaving a charge residual of $\sim 0.2\%$. We have masked these ghosts manually in the weight images as they did not average out entirely due to the repeated dither pattern.

The same star, located in array #1, also causes significant negative crosstalk in one of the four output channels of array #1. Contrary to image persistence, the position of this crosstalk is fixed with respect to the star and thus does not average out. We masked it manually in the weight maps.

Other memory effects exist in some GSAOI arrays. This is particularly noticeable in the low resolution ($0''.06 \text{ pixel}^{-1}$) stack of MACS J0416.1-2403 with its high S/N ratio because of the effective 3×3 re-binning. Darker spots with a maximum amplitude of twice the background noise level (Fig. 4) mirror the dither pattern. Only some parts of the arrays are affected, as neighboring sources of similar brightness do not cause ghosting. The origin of this behavior is still under investigation. It is of minor concern as it rarely coincides with images of astrophysical objects. The non-repetitive dither pattern used for Abell 2744 (and Abell 370) fully suppresses this feature.

3.5. Astrometric calibration with Scamp

THELI uses *Scamp* (Bertin 2006) for the astrometric calibration, and the discussion below is specific in this context. Nonetheless, our results should provide a useful reference point when solving GSAOI astrometry with other software.

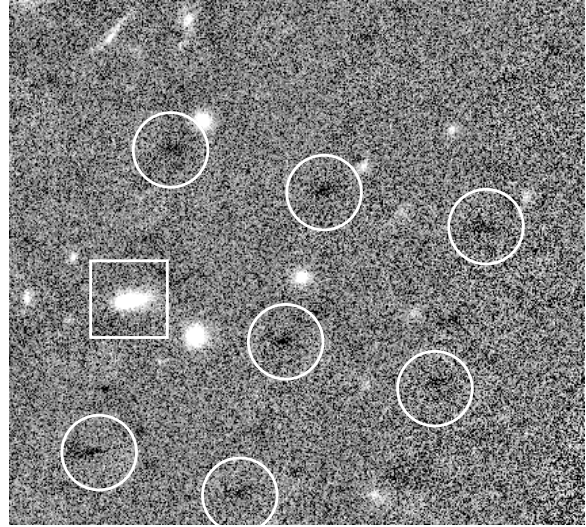


Fig. 4.— A low-level memory effect (white circles) appears in certain areas of the GSAOI detectors. In this example it is caused by the galaxy marked with a white square. A neighboring object of similar brightness does not trigger the effect.

3.5.1. Input catalogs and Scamp settings

The setup error described in Sect. 2 resulted in an offset of $24''$, which is not reflected in the headers of the archival data taken on 2014-01-13/14. The CRVAL1/2 header keywords were manually corrected to within $\sim 1''$, i.e. the typical WCS uncertainty in raw GSAOI data. We then loaded *SExtractor* source catalogs into *Scamp* (v2.0.1), using a low detection threshold per pixel (`DETECT.THRESH = 1.2`) to maximize the number of usable sources. A minimum of `DETECT.MINAREA = 20` pixels above this threshold was required to form a valid object (rejecting spurious sources, and because GSAOI data are oversampled). This resulted in an average of 11 ± 5 (8 ± 3) detections (mostly galaxies) per array for MACS J0416.1-2403 (Abell 2744). *Scamp* uses its own internal S/N thresholds for object filtering. A very low setting is required to retain a sufficient number of objects for successful matching with the reference catalog. The final astrometric solution was obtained using a refined median estimate of the relative chip positions and orientations from all exposures in a night (`MOSAIC.TYPE = FIX_FOCALPLANE`), and a 2nd order distortion model. We reproduce all relevant parameter settings in Table 2. A typical distortion model is shown in Fig. 5, re-

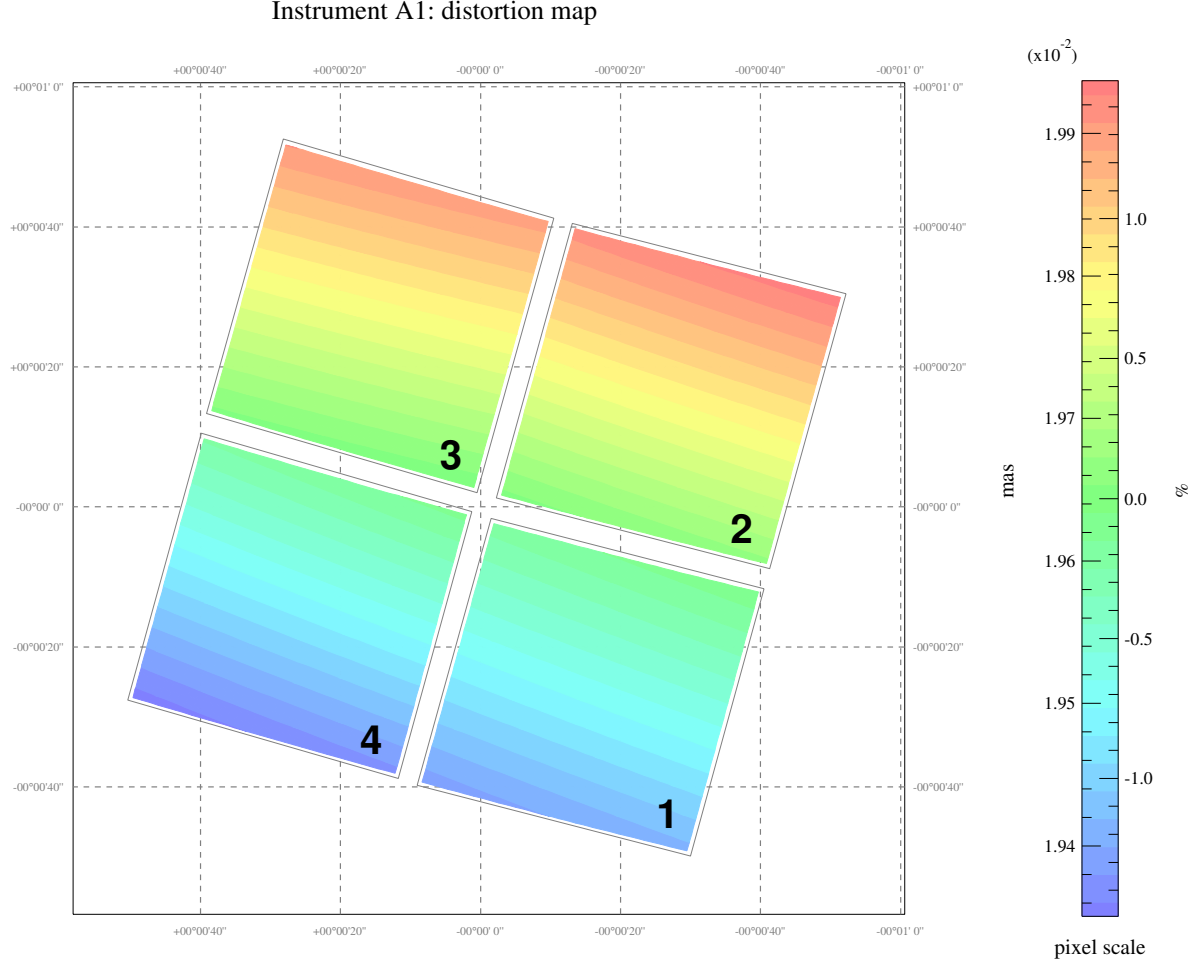


Fig. 5.— Typical GSAOI distortion model. Note that *Scamp* calculates plate scale variations independently for each of the four arrays. The distortion is recovered reliably from the dithered data despite the low source density.

vealing a plate scale variation of 3%.

3.5.2. The need for secondary reference catalogs

Astrometry with GSAOI is non-trivial. First, there is a large discrepancy between the angular resolutions of GSAOI and common all-sky astrometric reference catalogs. A single reference source (stellar or non-stellar) may be resolved into several components by GSAOI. Second, the AO field of view is comparatively small and at high galactic latitude no (or only a few) reference sources are available. Third, GSAOI works in the near-infrared, whereas reference catalogs are mostly based on optical data. This often results in very low densities of the reference catalog in highly

reddened areas (2MASS is an exception, but it is comparatively shallow). In our case with mostly extragalactic sources, bluer reference catalogs are susceptible to sub-structures in galaxies whereas the redder science data mainly detect the galactic bulges and nuclei. Forth, GeMS introduces a significant field distortion by means of its optical relay (consisting of two off-axis parabolic mirrors). Fortunately, this distortion is static and, as we show below, it can be measured reliably even for sparse data.

Lastly, the distortion correction is imperfect as the wavefront correction is a function of the atmospheric turbulence profile and e.g. the brightness of the LGS. The latter depends on the laser performance, the align-

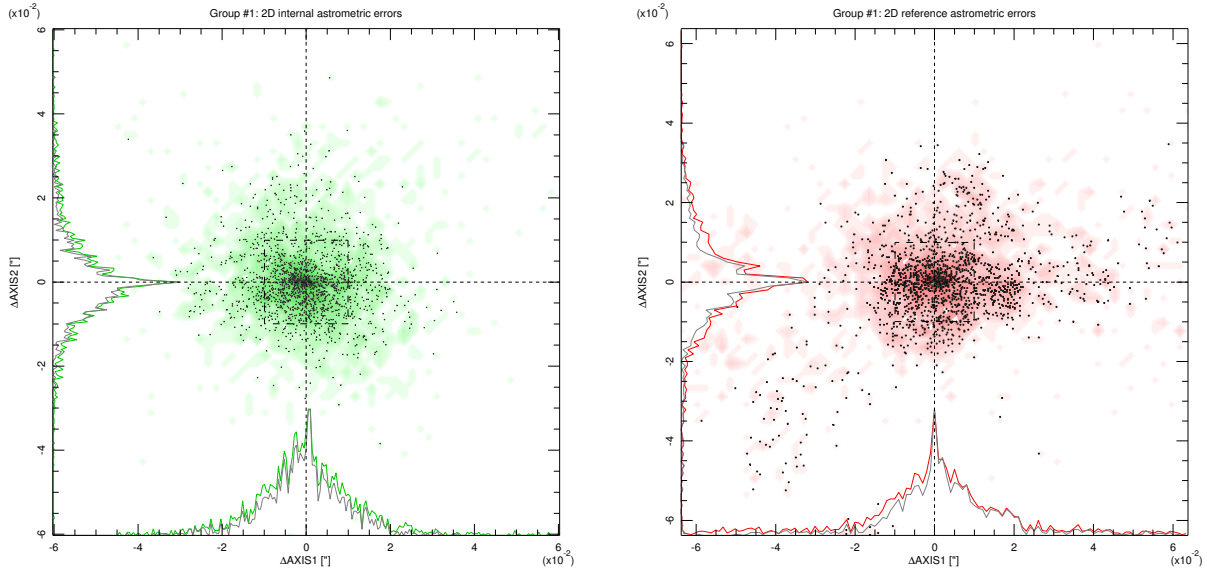


Fig. 6.— Shown are the internal astrometric residuals (i.e. between exposures, left panel) and the external residuals (with respect to the *VLT/HAWK-I* K_s -band image; right panel). Sub-pixel accuracy is achieved in both cases, despite only a few dozen low-S/N detections of extended sources have been available for the calibration.

ment of the laser beam transfer optics, and also the atmosphere’s sodium layer (which has a strong seasonal dependence and is replenished by meteor showers). This affects mostly investigations where high precision astrometry is required. For more details see e.g. Cameron et al. (2009); Ammons et al. (2013); Neichel et al. (2014a).

For our purposes, the key to successful WCS matching and sufficiently good distortion modeling are deeper secondary (or even tertiary) reference catalogs (see also Schirmer 2013), ideally constructed from observations at similar wavelengths.

3.5.3. External astrometry

For both galaxy clusters we tried different reference catalogs constructed from (1) the *HST/ACS* F814W images (the *HST/WFC3* near-infrared data do not fully overlap with the GSAOI pointings), and (2) deep *VLT/HAWK-I* K_s -band observations (PI: Brammer, ESO program ID: 092.A-0472; image seeing $0''.29$ – $0''.37$). In case of MACS J0416.1-2403 we also tested a R -band image taken with the Wide Field Imager (*WFI*) at the 2.2m MPG/ESO telescope (Grün et al. 2014, ESO program ID: 083.A-9026; image seeing $0''.95$). The co-added ground-based data were created with THELI and calibrated against 2MASS

(Skrutskie et al. 2006).

Matching was successful for all three reference catalogs. However, calibration against the *WFI* data caused large residuals (30 – 70 milli-arcseconds) and we do not consider it further. *HST/ACS* and *VLT/HAWK-I* catalogs have given similar results for MACS J0416.1-2403. For Abell 2744 we could not obtain a good distortion correction for array #2 with the *HST/ACS* catalog.

Particularly noteworthy is that the *VLT/HAWK-I* catalog resulted in external residuals of 12 – 14 milli-arcseconds, whereas for *HST/ACS* we got 6 – 9 milli-arcseconds. This is not surprising as the *HST* data have smaller measurement errors for the centroids due to the high angular resolution. However, the nominal *Scamp* χ^2 values for the *VLT/HAWK-I* fit have been about 1 – 6 per image for both clusters, whereas for *HST/ACS* we have found $\chi^2 = 10$ – 30 for MACS J0416.1-2403, and $\chi^2 = 30$ – 100 for Abell 2744. The *HST* data are significantly bluer ($0.8\mu\text{m}$) than the *VLT* images ($2.2\mu\text{m}$) and thus more susceptible to sub-structures in the galaxies. The effect is immediately visible when over-plotting both reference catalogs over the GSAOI exposures. The centroids measured in the *VLT/HAWK-I* data, taken in the same filter as the GSAOI images, align better for a larger number of objects. The higher

χ^2 for Abell 2744 is likely the result of a larger fraction of late-type galaxies (spirals and edge-on disks). The GSAOI pointing is further away from the cluster center than for MACS J0416.1-2403 (compare Figs. 10 and 11), and thus the effect of sub-structure is perhaps more pronounced.

We base our final external WCS calibration on the *VLT/HAWK-I* data, which in turn have been calibrated against 2MASS. Note that in v1.0 of the *HST* data systematic WCS offsets of $0''.17$ and $0''.40$ are present for MACS J0416.1-2403 and Abell 2744, respectively. Corrections for the *HST* headers are as follows:

$$\Delta\text{CRVAL1} = +5.0 \times 10^{-5} \text{ (MACS J0416.1)} \quad (2)$$

$$\Delta\text{CRVAL2} = -0.6 \times 10^{-5} \text{ (MACS J0416.1)} \quad (3)$$

$$\Delta\text{CRVAL1} = -5.8 \times 10^{-5} \text{ (Abell 2744)} \quad (4)$$

$$\Delta\text{CRVAL2} = +9.4 \times 10^{-5} \text{ (Abell 2744)} \quad (5)$$

3.5.4. Internal astrometry

The χ^2 did not improve when switching from a 2nd to a 3rd order distortion polynomial. The higher order solution is poorly constrained, given the small number of sources, and significant discontinuities in the pixel scale occurred across array boundaries. Thus we have selected the simpler 2nd order hypothesis. The internal and external residuals for MACS J0416.1-2403 are shown in Fig. 6 and measure 10 and 13 milli-arcseconds, respectively (same for Abell 2744). This is equivalent to half a GSAOI pixel and should be sufficient for most purposes of these particular data sets. The dominating factors limiting the fits are the low source densities and the large measurement uncertainties of the source centroids (0.1 – 0.3 pixels or 2 – 6 milli-arcseconds for galaxies).

Astrometric solutions have been obtained on a nightly basis. We have also tested a common distortion model for all nights, and find it to be inferior. This is because the large angular offsets between the base positions of different nights introduce different distortion patterns as the NGS and LGS configurations move with respect to each other (Neichel et al. 2014a,b; Rigaut et al. 2014). For another test we have split the nightly sequences into blocks of 30 minutes to sample a variable distortion component caused by flexure due to a changing gravity vector (Neichel et al. 2014a). This effect becomes important when high precision relative astrometry (on the order of one milli-arcsecond and below) is required across the field (Neichel et al. 2014a,b). We find that for blocks with

Table 2: Useful *Scamp* parameter ranges for our GSAOI data (see the *Scamp* manual for details)

Parameter	Setting
POSANGLE_MAXERR	0.5
POSITION_MAXERR	0.035
PIXSCALE_MAXERR	1.03
DISTORT_DEGREE	2
ASTREF_WEIGHT	1...10
SN_THRESHOLDS	2...4, 10...20
STABILITY_TYPE	INSTRUMENT
MOSAIC_TYPE	FIX_FOCALPLANE
CROSSID_RADIUS	0.1...0.6
MATCH	Y

good AO-corrected seeing (80 milli-arcseconds) the internal residuals decrease from 10 to 6 – 8 milli-arcseconds, whereas for other blocks the quality of the fit was unchanged or worse. We thus decided to use the more stable nightly fits instead.

Better performances are hard to reach with GeMS at high galactic latitude with few low S/N detections per array, almost all of which extended, and just a single NGS. In comparison, for dense stellar fields such as NGC 1851 with 500 – 1000 sources per array with $S/N > 10$ – 100, optimal NGS asterisms and in the absence of dithering, GeMS delivers relative astrometric accuracies of 0.4 milli-arcseconds and better (Neichel et al. 2014a; Ammons et al. 2013; Rigaut et al. 2012).

3.6. Photometric calibration

THELI normalizes the gains of multi-chip cameras to the array with the lowest gain, i.e. array #2 in case of GSAOI. The co-added images are scaled in ADU s^{-1} . Transformation from VEGA to AB magnitudes in the K_s -band filter is obtained by adding 1.85 mag.

3.6.1. Transparency

Sky transparency was good, yet somewhat unstable during all observing nights (see Fig. 7). The instabilities were caused by a high inversion layer trapping significant amounts of humidity above the observatory. Such conditions may be difficult to recognize at night by observers. Other factors that contribute to the scattering between exposures are errors in the gain determination of the four arrays of 0.5% – 1.0%, and small differences in their quantum efficiencies. In Carrasco et al. (2012) we have observed similar uncertainties for

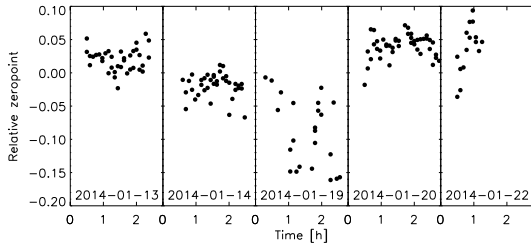


Fig. 7.— MACS J0416.1-2403: Variation of the relative photometric zero-points between exposures.

various stellar and non-stellar fields.

3.6.2. Absolute zero-point

For the absolute photometric calibration (MACS J0416.1-2403) two standards from the MKO catalog (Leggett et al. 2006) were observed on 2014-01-13 at airmasses 1.13 and 1.35, 1h and 4h after the last science exposure was taken. Assuming that the mean transparency has not changed during the night, we find a photometric zero-point of $ZP = 25.62 \pm 0.06$ mag (VEGA). This value is based on a linear two parameter fit for the zero-point and the extinction coefficient. We have neglected a small color term (~ 0.02 mag) between the GSAOI K_s -band filter and the K -band filter used for the MKO system (Leggett et al. 2006). The uncertainty of 0.06 mag includes the nominal uncertainty of the fit, contributions from the slightly non-photometric conditions and the uncertainties of the detector characteristics. For comparison, the only non-saturated star in the area detected by 2MASS has a K_s -band magnitude of 15.36 ± 0.19 mag (error from 2MASS photometry) after transformation to the MKO system, compared to 15.42 mag measured in our data.

To verify this calibration, we have re-observed MACS J0416.1-2403, Abell 2744 and a series of standard stars in K_s -band in a photometric night using the Flamingos-2 near-infrared imager at Gemini South. This independent Flamingos-2 calibration falls within 0.002 ± 0.02 mag of the 2MASS field photometry. Aperture photometry of common sources in the combined Flamingos-2 and GSAOI data did not reveal an offset.

3.6.3. Limiting magnitude

The depth of the co-added images vary across the field due to the dithered multi-chip data and can be as-

essed by means of the released coadded weight maps. Another factor that becomes important (compared to classical imaging) is that most of the accessible faint field galaxies in these data have intrinsic sizes smaller than the natural seeing disk ($0''.5$ - $0''.7$), but larger than the AO corrected seeing ($0''.08$). Therefore, a compact galaxy will benefit more from the AO correction than an equally bright but more extended galaxy. This dependence of the field depth as a function of source FWHM is difficult to model due to the field galaxies' mostly irregular morphologies, and we ignore it hereafter.

We cannot estimate the depth based on field stars as only a few point sources are found near MACS J0416.1-2403, none of which are near the detection limit. Instead, we use compact (yet extended) galaxies with half-light radii $\leq 0''.15$ in the deep medium resolution stack (see Sect. 4). Based on the distribution of magnitude errors, we measure a 10σ detection limit of $K_s = 22.4 \pm 0.2$ mag (VEGA) and extrapolate a 5σ limit of 23.8 ± 0.4 mag (25.6 ± 0.4 AB mag). The depth of the intermediate Abell 2744 data has not yet been determined as only 25% of the data have been taken (and in below average seeing conditions).

4. Summary and data release

The Gemini Frontier Fields Campaign complements *HST* observations redwards of $1.6\mu\text{m}$ for three galaxy clusters, MACS J0416.1-2403, Abell 2744 and Abell 370. Using GeMS/GSAOI, the first MCAO system in use at an 8m telescope, near diffraction-limited images on angular scales larger than $1''$ are obtained in K_s -band. We make the fully calibrated co-added images and weights publicly available⁶. This paper describes the observations and data reduction of the first two clusters observed, MACS J0416.1-2403 (complete) and Abell 2744 (incomplete). Abell 370 is scheduled for observation in 2015.

We release different co-added images resampled to $0''.02$, $0''.03$ and $0''.06 \text{ pixel}^{-1}$ (high, medium and low resolution stacks). The first preserves the native pixel scale of GSAOI, whereas the other two use identical plate scales and image geometries as the *HST* data release (their v1.0).

Natural seeing conditions have varied during the observing nights for MACS J0416.1-2403. We provide two different versions for the high and medium

⁶<http://www.gemini.edu/node/12254/>

Table 3: Summary of the released co-added data. The FWHM is the mean seeing measured within $1'$ of the NGS. Note that the Abell 2744 data will be incremented as by the time of writing only 25% of the planned data have been taken.

Stack name	Filter	Pixel scale	t_{exp} [s]	FWHM
MACS_J0416.1-2403_GSAOI_0.02_deep.fits	K_s	$0''.02$	15720	$0''.085$
MACS_J0416.1-2403_GSAOI_0.02_seeing.fits	K_s	$0''.02$	6600	$0''.077$
MACS_J0416.1-2403_GSAOI_0.03_deep.fits	K_s	$0''.03$	15720	$0''.086$
MACS_J0416.1-2403_GSAOI_0.03_seeing.fits	K_s	$0''.03$	6600	$0''.080$
MACS_J0416.1-2403_GSAOI_0.06_deep.fits	K_s	$0''.06$	18600	$0''.095$
A2744_GSAOI_0.02_v0.1.fits	K_s	$0''.02$	4800	$0''.100$
A2744_GSAOI_0.03_v0.1.fits	K_s	$0''.03$	4800	$0''.105$
A2744_GSAOI_0.06_v0.1.fits	K_s	$0''.06$	4800	$0''.120$

resolution stacks, optimized for seeing (35% of all exposures) and depth (85%). For the low resolution stack only one deep version is provided comprised of all usable exposures, as PSF anisotropies and softer seeing become insignificant. For Abell 2744 all currently available exposures were used. Table 3 summarizes the key properties of the stacked images.

Only one NGS is available for each of the galaxy clusters and GeMS/GSAOI. This results in increasing PSF variations and FWHM as a function of separation from the NGS (Fig. 9). The performance variation over the field is predicted well based on numerical simulations, which are available in the Gemini Observing Tool⁷. With a FWHM of $0''.07$ – $0''.10$ we improve upon *HST/WFC3*’s angular resolution by a factor of two, albeit over a smaller field of view ($100'' \times 110''$). We reach a 5σ depth for extended sources of $K_s^{\text{lim}} = 25.6$ AB mag. This demonstrates that MCAO at Gemini South works well even for high galactic latitude fields where natural guide stars are scarce, opening a new window onto the distant Universe. We have also shown that current data reduction techniques, developed for classical imaging, are well suitable for this type of MCAO data.

4.1. Future work

In 2015 and 2016 the MCAO system at Gemini Observatory will receive two very significant upgrades. First, new NGS wavefront sensors enable us to guide on $V \sim 17.5$ mag stars (currently $V \sim 15$ mag), which will dramatically increase the sky coverage, and the number of targets for which triangular guide star constellations are available. Second, funding has been

secured for the purchase of a Topica (Karpov et al. 2011) laser offering increased LGS brightness, easier maintenance and operation, and lower losses due to simplified beam transfer optics.

Acknowledgments

We thank Nancy Levenson and Markus Kissler-Patig for granting us directors’ discretionary time, and the anonymous referee for the valuable comments that helped us improve our paper. This work utilizes gravitational lensing models produced by PIs Brada, Ebeling, Merten & Zitrin, Sharon, and Williams funded as part of the *HST* Frontier Fields program conducted by STScI. STScI is operated by the Association of Universities for Research in Astronomy, Inc. under NASA contract NAS 5-26555. The lens models were obtained from the Mikulski Archive for Space Telescopes (MAST). The astrometric calibrations of the GSAOI data have been based on secondary reference catalogs derived from *VLT/HAWK-I* observations, made with ESO Telescopes at the La Silla Paranal Observatory under program ID 092.A-0472.

REFERENCES

- Ammons, S. M., Bendek, E., Guyon, O., et al. 2013, in Proceedings of the Third AO4ELT Conference, ed. S. Esposito & L. Fini
- Bertin, E. 2006, in ASP Conf. Ser., Vol. 351, ADASS XV, ed. C. Gabriel, C. Arviset, D. Ponz, & S. Enrique, 112
- Bertin, E. & Arnouts, S. 1996, A&AS, 117, 393
- Cameron, P. B., Britton, M. C., & Kulkarni, S. R. 2009, AJ, 137, 83

⁷<http://www.gemini.edu/sciops/instruments/gems/gems-performance?q=node/11864#Asterism.visualization>

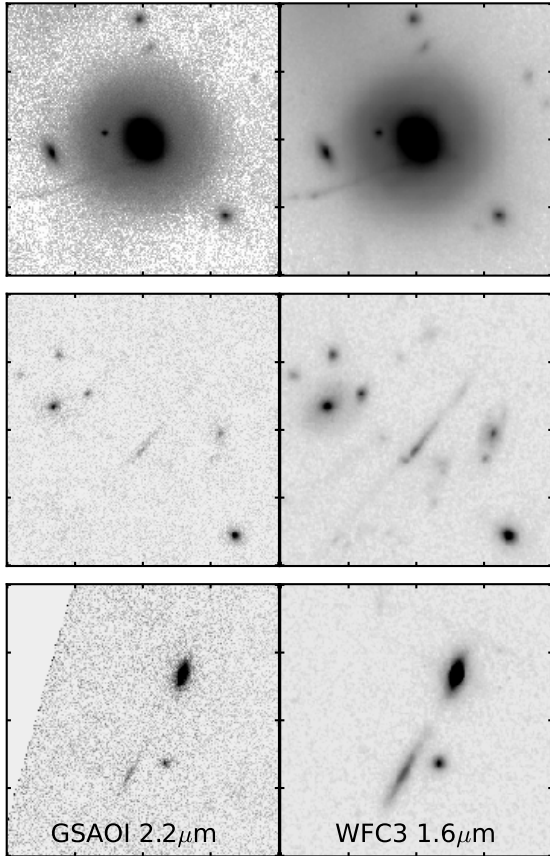


Fig. 8.— Comparison of strongly lensed features in MACS J0416.1-2403 seen by GSAOI and *HST/WFC3*. The areas measure $12'' \times 12''$, and have North up and East left.

Carrasco, E. R., Edwards, M. L., McGregor, P. J., et al. 2012, in Society of Photo-Optical Instrumentation Engineers (SPIE) Conference Series, Vol. 8447, Society of Photo-Optical Instrumentation Engineers (SPIE) Conference Series

Ebeling, H., Ma, C.-J., & Barrett, E. 2014, *ApJS*, 211, 21

Ellerbroek, B. & Rigaut, F. 2000, *Nature*, 403, 25

Erben, T., Schirmer, M., Dietrich, J., et al. 2005, *AN*, 326, 432

Grün, D., Seitz, S., Brimiouille, F., et al. 2014, *MNRAS*, 442, 1507

Karpov, V., Protopopov, V., Clements, W., et al. 2011, in Second International Conference on Adaptive Optics for Extremely Large Telescopes, 52

Leggett, S. K., Currie, M. J., Varricatt, W. P., et al. 2006, *MNRAS*, 373, 781

McGregor, P., Hart, J., Stevanovic, D., et al. 2004, *Proc. SPIE*, 5492, 1033

Neichel, B., Lu, J. R., Rigaut, F., et al. 2014a, *ArXiv e-prints*

Neichel, B., Rigaut, F., Vidal, F., et al. 2014b, *MNRAS*, 440, 1002

Owers, M. S., Randall, S. W., Nulsen, P. E. J., et al. 2011, *ApJ*, 728, 27

Postman, M., Coe, D., Ford, H., et al. 2011, in Bulletin of the American Astronomical Society, Vol. 43, American Astronomical Society Meeting Abstracts #217, 227.06

Ragazzoni, R., Marchetti, E., & Valente, G. 2000, *Nature*, 403, 54

Richard, J., Jauzac, M., Limousin, M., et al. 2014, *MNRAS*, 444, 268

Rigaut, F., Neichel, B., Boccas, M., et al. 2012, in Society of Photo-Optical Instrumentation Engineers (SPIE) Conference Series, Vol. 8447, Society of Photo-Optical Instrumentation Engineers (SPIE) Conference Series

Rigaut, F., Neichel, B., Boccas, M., et al. 2014, *MNRAS*, 437, 2361

Schirmer, M. 2013, *ApJS*, 209, 21

Skrutskie, M. F., Cutri, R. M., Stiening, R., et al. 2006, *AJ*, 131, 1163

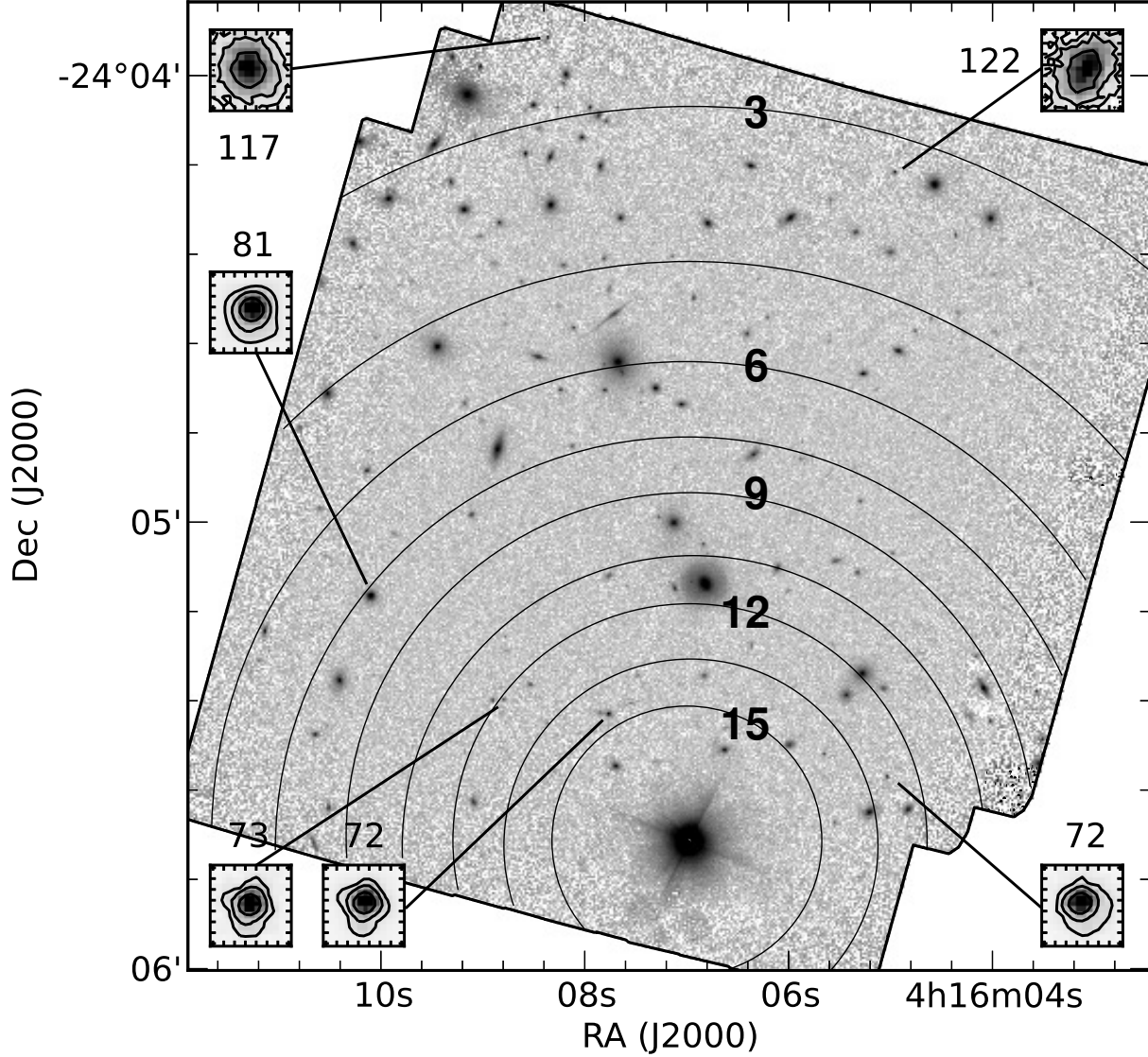


Fig. 9.— PSF of the 6 brightest field stars in our medium resolution *good seeing* stack. The extent of the small boxes is $0''.3 \times 0''.3$, and the contour levels therein correspond to 0.1, 0.2 and 0.5 times the stars' peak fluxes. The PSF is fairly uniform and increases with growing distance from the single natural guide star (bright source at the bottom). Only the upper right star displays significant ellipticity. The numeric values next to each box correspond to the direct FWHM in milli-arcseconds, measured with IRAF/imexam. The large concentric contours around the natural guide star show the expected Strehl ratio for the given guide configuration, increasing from 3% to 15%. The expected average Strehl ratio is 6.9%, corresponding to a FWHM of 90 mas, consistent with the delivered image quality. For reference, the diffraction limited FWHM for GeMS/GSAOI in K_s -band is 55 milli-arcseconds (Neichel et al. 2014b).

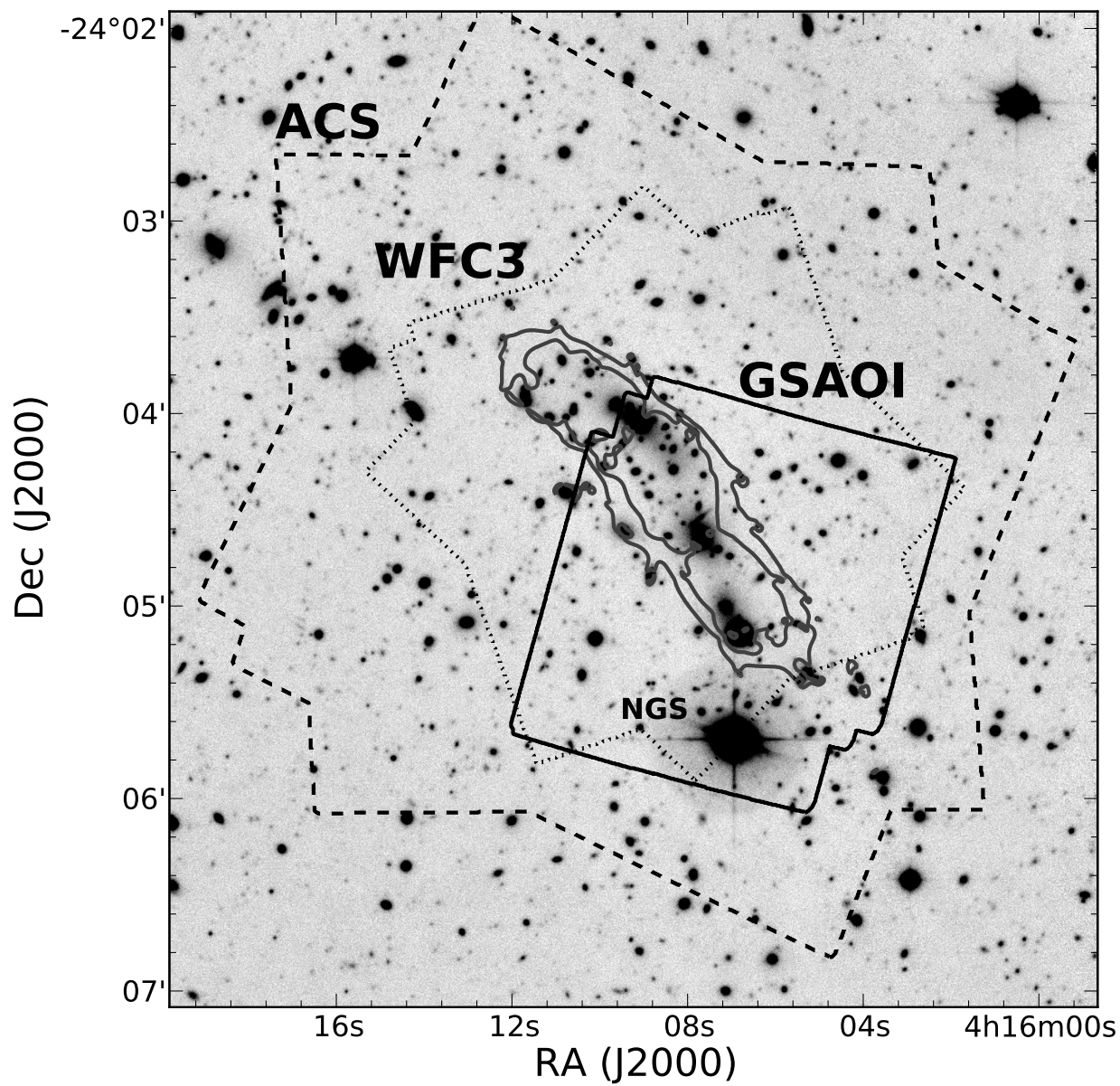


Fig. 10.— Layout of the *HST/ACS*, *HST/WFC3* and GSAOI fields for MACS J0416.1-2403. The (smoothed) gray contours indicate the area where a magnification higher than 20 is expected for a $z = 9$ source (from Richard et al. 2014). The NGS has been labeled, too.

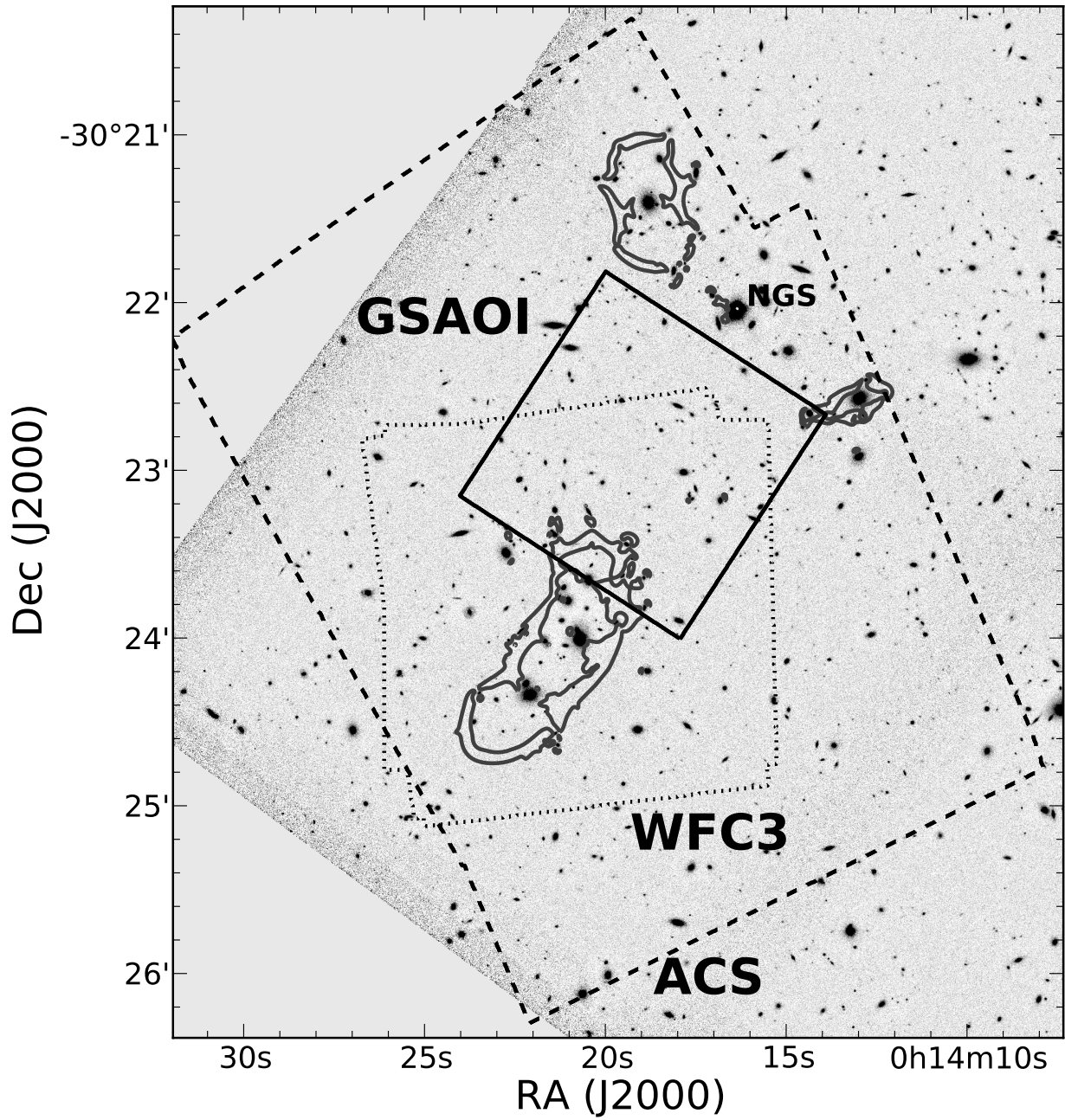


Fig. 11.— Same as Fig. 10, for Abell 2744. Note that the NGS is too far away from the cluster center for GSAOI to cover the area with highest magnification.

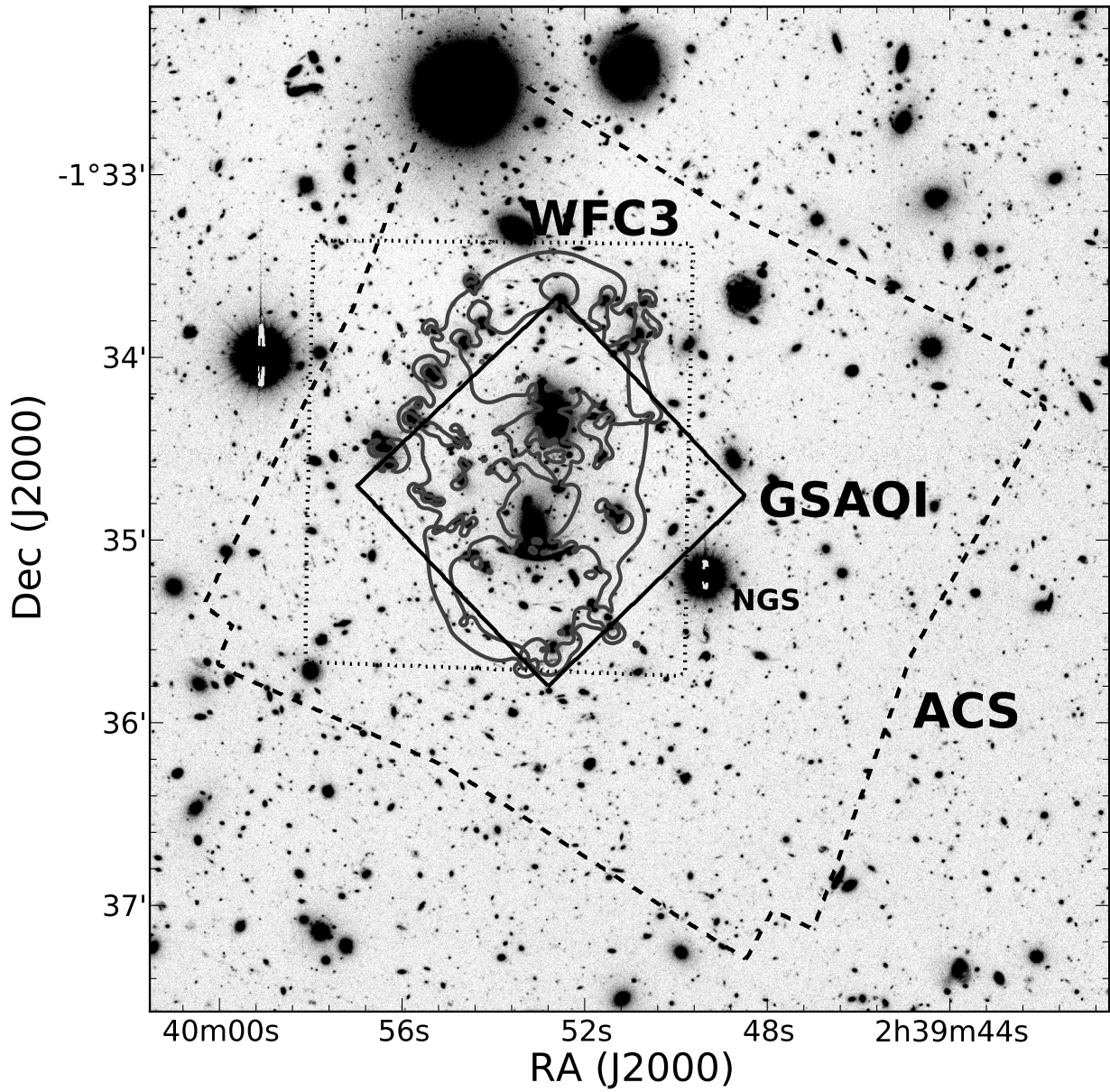


Fig. 12.— Same as Fig. 10, for Abell 370. Note that the *HST* layouts are subject to change as further imaging is pending. Likewise, the final GSAOI pointing has not yet been chosen.